Comparative Analysis of Single-antenna and Dual-antenna GNSS Configurations in Mobile Mapping Systems

Taweeyossak, A.,[1] Srinara, S.[2] and Satirapod, C.[1*]
[1]Mapping and Positioning from Space (MAPS) Technology Research Center, Department of Survey Engineering, Faculty of Engineering, Chulalongkorn University, Bangkok 10330, Thailand
E-mail: fern.airt21@gmail.com, chalermchon.s@chula.ac.th[1]*
[2]Department of Civil Engineering, University of Phayao, Phayao 56000, Thailand
E-mail: surachet.sr@up.ac.th
**Corresponding Author*

DOI: https://doi.org/10.52939/ijg.v22i2.4779

Abstract
Mobile mapping systems (MMS) have become increasingly important in surveying and geospatial data acquisition, offering efficient and flexible solutions for collecting spatial information. While most commercial MMS platforms employ single-antenna configurations, dual-antenna setups have shown potential for improving positional accuracy and heading stability. This study investigates the comparative performance of single-antenna and dual-antenna configurations in post-processed kinematic (PPK) processing with tightly coupled integration. Data were collected using a custom-built MMS equipped with a Fiber Optic Gyroscope Inertial Navigation System (FOG-INS), dual GNSS antennas, and an odometer across two contrasting environments: a dense urban area with severe signal obstruction and an open-sky area with minimal GNSS obstruction. The analysis focused on yaw and positional differences between the two configurations to evaluate methodological implications and practical significance. Results indicate that in urban environments, the maximum difference in yaw values between single-antenna and dual-antenna processing was 0.107° with an average difference of 0.049° along the entire path and maximum positional differences in 2D and 3D about 1.931 meters and 2.245 meters, respectively. In contrast, for the second experiment (open-sky area), the maximum yaw difference was 0.008° with an average of 0.002°, and positional differences were limited to the millimeter range. These findings demonstrate that dual-antenna configurations enhance the robustness and reliability of MMS data collection under degraded GNSS conditions, contributing to improved mapping performance and system stability. The outcomes of this research provide a practical framework for selecting antenna configurations and data acquisition strategies suited to varying environmental constraints, while future studies are encouraged to explore alternative coupling schemes and advanced algorithms to further optimize system accuracy.

Keywords: Dual-antenna, Mobile Mapping System, Post-Processing Kinematic (PPK), Single-Antenna, Tight-Coupling

1. Introduction

Mobile Mapping System (MMS) is a system used for surveying to create virtual three-dimensional maps. It significantly improves the efficiency and speed of fieldwork and reduces the number of personnel required for surveying large areas. The MMS can be installed on various platforms, such as cars, planes, drones, boats, backpacks, or even handheld [1]. This versatility allows for a wide range of applications. A Mobile Mapping System fundamentally consists of two main subsystems: the Global Navigation Satellite System (GNSS) and the Inertial Navigation System (INS). This integration is designed to leverage the strengths of each sensor to compensate for the weaknesses of the other [2]. The primary sensors currently used in these systems include an Inertial Measurement Unit (IMU), a GNSS receiver, a Light Detection and Ranging (LiDAR) sensor, and a 360-degree panorama camera. To ensure the accuracy and reliability of the results, it is essential to precisely calibrate the installed equipment, including the vehicle's trajectory [3] and the point cloud data, especially to prevent errors in

overlapping areas [4]. The data obtained from the MMS sensors can be applied to various tasks, such as mapping, construction, Geographic Information System (GIS) work, and advanced data analysis. For instance, point cloud data and/or images can be used to classify objects of interest like utility poles, traffic signs [5], trees [6], and roads, as detailed in [7] and [8]. This analyzed data can then be used for urban planning or applied in Smart City initiatives.

In Thailand, the use of Mobile Mapping Systems is becoming widespread in both government and private sectors. Most systems are equipped with a single GNSS antenna. The selection of applications has not yet adequately considered the differential effects of data acquired using single-antenna versus dual-antenna Mobile Mapping Systems in diverse environmental contexts. However, the Hydro Informatics Institute (Public Organization) (HII) [9] developed its own MMS to conduct research on sensor fusion and to create a system that can be effectively utilized in the country. A key advantage of this self-developed system is the flexibility to select sensors based on specific characteristics and budget. The HII's MMS featured a dual GNSS antenna setup, which leverages a GNSS compass to provide additional directional data for the vehicle, thereby increasing the accuracy of the results. The benefits of using a dual-antenna system over a single-antenna one has also been explored in numerous international studies [10][11][12][13] and [14].

Therefore, research aims to compare the performance of single-antenna versus dual-antenna Mobile Mapping Systems (MMS). We used a single, custom-built MMS not a commercial one to minimize sensor-related discrepancies. The same dataset was processed twice, once with a single-antenna setting and once with a dual-antenna setting, to specifically compare the resulting vehicle trajectory from Post-Processing Kinematic (PPK) with tightly-coupled. The study was conducted in both an urban environment, where satellite signals are obstructed, and an open-sky area. The findings highlight the differences in results between the two configurations, providing valuable insights for future research and guiding the appropriate selection of MMS types for various applications and environments.

2. Materials and Methods

2.1 Custom-Built Mobile Mapping System

The data from the MMS used in this research is sourced from a custom-built mobile mapping system (Figure 1(a)). This system consists of an Inertial Measurement Unit (IMU), specifically an SBG Navsight Horizon model INS with FOG (Fiber Optic Gyro) technology (Table 1) known for its superior durability and resistance to vibration compared to MEMS-based INS [15], configured to a data frequency of 200 Hz. It also includes a Global Navigation Satellite System (GNSS) receiver, a Septentrio TWIVSP6037L (Table 2) dual-antenna model with an antenna separation of approximately 1.90 meters (Figure 1(b)), an odometer or Distance Measurement Instrument (DMI) (Table 3), a 2-return LiDAR, and a Ladybug panoramic camera. Data was collected at speeds not exceeding 40 kilometers per hour according to project conditions. The preceding description encompasses all sensors integrated within the Mobile Mapping System; however, data from the LiDAR and panoramic camera are not utilized as the primary input for this research.

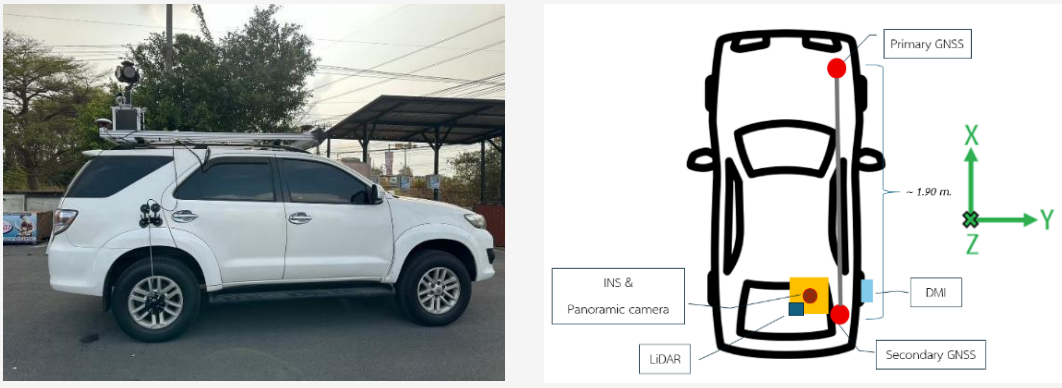

(a) (b)

Figure 1: Custom-built Mobile Mapping System (a) Side view and (b) Top view

Table 1: INS specifications used in this research

INS specifications		
Brand / Model		SBG Navsight Horizon model INS with FOG grade
Dimensions		94 x 94 x 177 mm.
Weight		1.32 kilograms
IP Rating		IP68
Frequency		200 Hz
PPK	Roll, Pitch Accuracy	0.004˚
	Heading Accuracy	0.008˚
	Horizontal Accuracy	1 cm. + 1ppm
PPK (Signal loss 60 seconds)	Roll, Pitch Accuracy	0.005˚
	Heading Accuracy	0.01˚
	Horizontal Accuracy	0.05 meters

Table 2: GNSS specifications used in this research

GNSS specifications	
Brand / Model	Septentrio TWIVSP6037L
Dimensions	170 (dia.) x 74.9 (h.) mm.
Weight	500 grams
IP Rating	IP69K
Frequency	1 Hz
Frequency coverage	GPS/QZSS-L1/L2/L5, QZSS-L6, GLONASS-G1/G2/G3, Galileo-E1/E5a/E5b/E6, BeiDou-B1/B2/B2a/B3, NavIC-L5 + L-Band correction services

Table 3: DMI specifications used in this research

DMI specifications	
Brand / Model	PEGASEM WSS4
Dimensions	108 x 43 x 30 mm.
Weight	310 grams
IP Rating	IP67
Output pulse rate	1600 ppr
Maximum Rotational Speed	3000 RPM

2.2 Study Area

Two study areas were chosen for this research (Figure 2). Each site represents a different operating environment, allowing for comparisons of the differences in results across sites. The first experiment served as a sample of a dense urban environment that poses significant challenges to satellite signal receiving during fieldwork with a mobile mapping system, which the dilution of precision (DOP) shown in the Figure 3. This area was located on Sukhumvit Road in Bangkok, where a sensor-equipped car was driven for approximately 30 kilometers under expressways and elevated train tracks. Field data was systematically collected in an urban area on April 29, 2024, during GPS Week 2312, spanning a duration of approximately 3 hours and 16 minutes, from 118477 to 130280 seconds. The extended duration of the data collection was primarily a consequence of the dense and congested traffic conditions, which significantly hindered the vehicle from maintaining a consistent speed. The collection process also included periods where the vehicle was stationary, with the heading estimation data being available for 75% of the total distance covered. The second experiment was chosen as a sample of an open-sky area with no significant obstacles or obstructions to satellite signal receiving, which the dilution of precision (DOP) shown in the Figure 4. The data collection took place in Laem Chabang Municipality, Chonburi Province, covering a distance of approximately 18 kilometers. Field data was collected in an open-field area on March 27, 2024 (GPS Week 2307), from 275410 to 279627 seconds, totaling approximately 1 hour and 10 minutes. The Dual GNSS-estimated heading data was available for 98% of the entire route. During the data acquisition runs, a base GNSS station was set up

to receive satellite signals. This base station served as the reference for data processing, with its coordinates referenced to the Royal Thai Survey Department's GNSS CORS network. The survey route was located within a 20-kilometer radius of the base station.

2.3 INS/GNSS Integration Systems

To overcome the limitations of stand-alone INS and GNSS, these systems are integrated to combine their advantages and achieve a more accurate and superior navigation solution [16].

2.3.1 Loose coupling

Loosely coupled data links operate independently, with the two systems physically separated in terms of their position, velocity, and attitude. To achieve optimal results, the data streams are minimally influenced by one another, and are then combined with the most appropriate estimates to produce the best possible outcome (Figure 5).

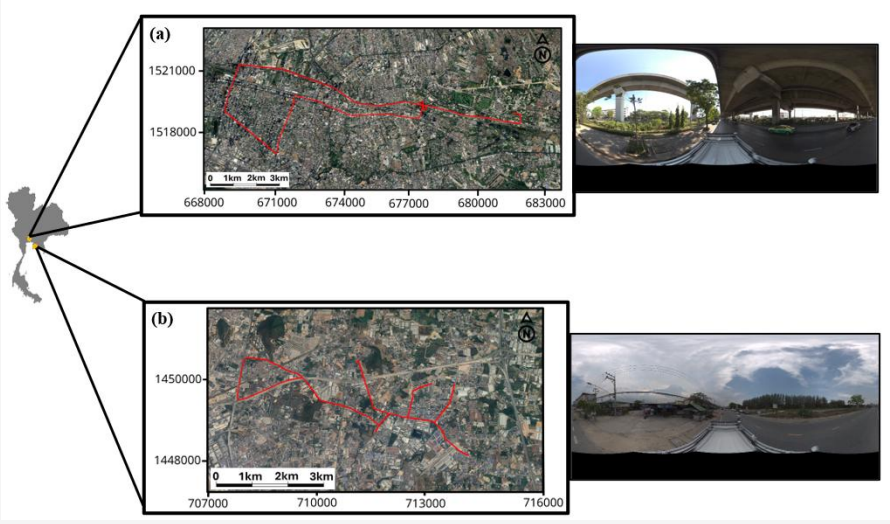

Figure 2: Overview of the study areas: (a) urban area (b) open-sky area (Coordinate System: WGS 84 / UTM Zone 47N)

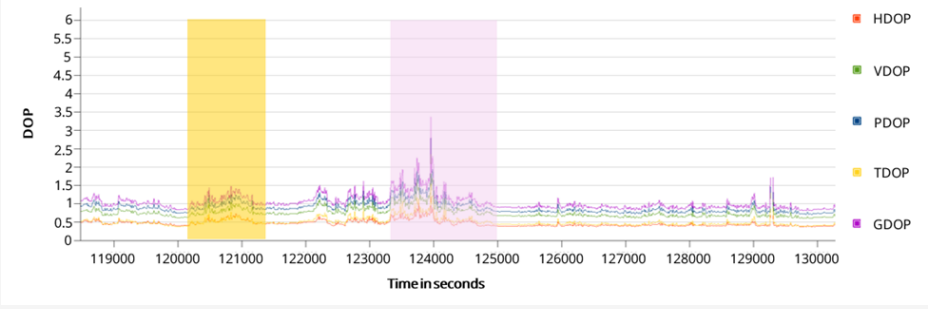

Figure 3: Dilution of precision (DOP) of urban area

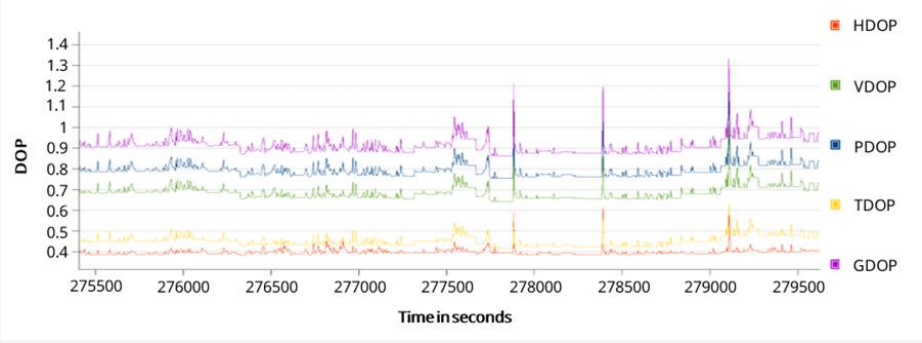

Figure 4: Dilution of precision (DOP) of open-sky area

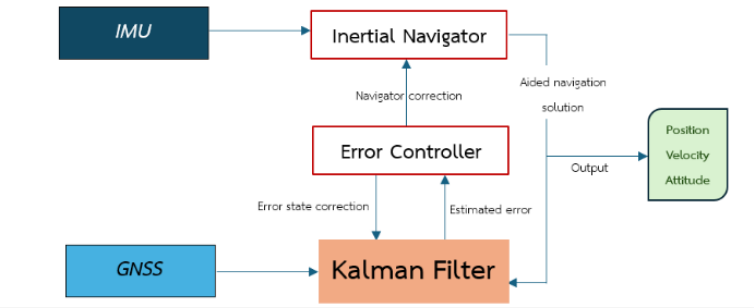

Figure 5: Loose coupling scheme (modified from [17])

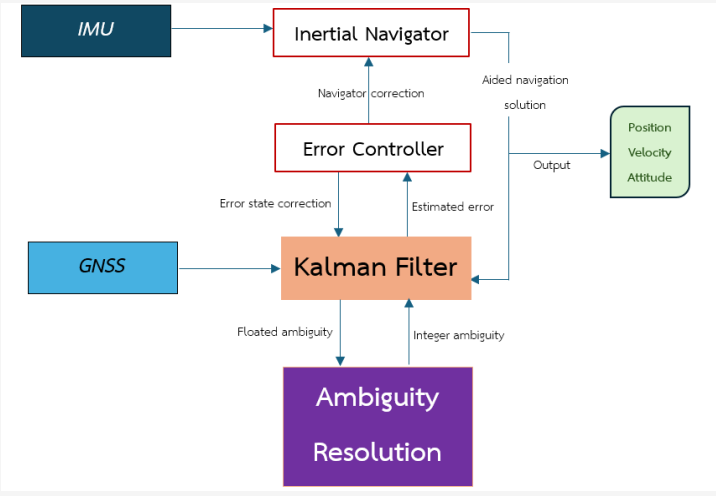

Figure 6: Tight coupling scheme (modified from [17])

2.3.2 Tight coupling

Tight coupling is a centralized data fusion method where the INS and GNSS sensors function as a foundational base. Combining GNSS and INS measurements enhances observability, reduces noise, and improves fault detection [18]. Data from these sensors are then interconnected, with the information from one directly influencing the other. This approach yields higher positional accuracy compared to loose coupling [19] and [20], although it requires more complex computations. In a study by [21], it was demonstrated that this algorithm provides a precise state estimation with a high data update rate. This capability allows for more effective adjustments to rotation and point cloud maps, even in cases where the LiDAR sensor has degraded or when testing is conducted in open, outdoor environments. In this research, a tightly coupled INS/GNSS integration method was chosen for data processing (Figure 6).

2.4 Euler Angle

Any three-dimensional orientation, as demonstrated by Euler, can be represented by a series of three rotations: Yaw, Pitch, and Roll. The Yaw indicates rotation around the Z-axis, which describes the vehicle's yaw or its left-to-right turning direction. Pitch represents rotation around the X-axis, illustrating the vehicle's forward or backward tilt. Lastly, the Roll signifies rotation around the Y-axis, which corresponds to the vehicle's side-to-side or lateral banking motion [22] and [23]. For this study, the analysis focused primarily on the yaw angle, as it is the most prominent parameter regarding the vehicle's direction and trajectory (Figure 7).

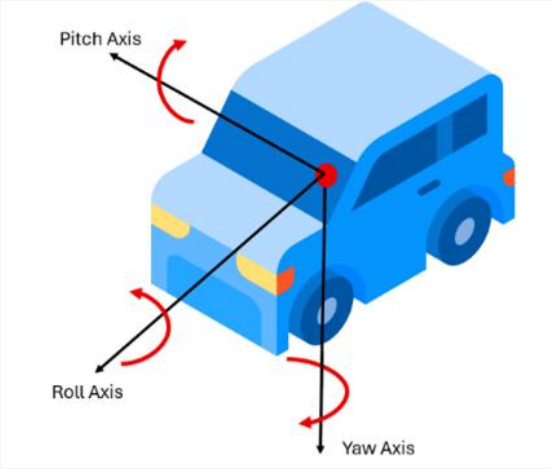

Figure 7: Vehicle attitude angles

2.5 Techniques for Determining Heading Values from GNSS/INS Systems

Determining a vehicle's heading using a magnetometer, or a device that measures magnetic fields, is the simplest method, as it directly utilizes the Earth's magnetic field to infer true north. However, this approach is highly susceptible to external interference from both natural and man-made magnetic materials. Consequently, a dual-antenna GNSS/INS system is employed to leverage the capabilities of a GNSS compass for more reliable heading determination. The GNSS compass calculates the heading angle by measuring clockwise from true north and estimates the tilt angle of the compass vector within a local East-North-Up (ENU) reference frame. This dual-antenna setup allows the vertical component's accuracy to approach that of the horizontal component, though its precision still relies on consistent satellite signal reception [11].

The GNSS compass method determines positional differences using carrier phase measurements to define the relative displacement of the GNSS compass vector within a local reference frame. A critical step in carrier phase measurement is resolving the integer ambiguity to ensure result accuracy. Once this integer ambiguity is resolved, the carrier phase measurement functions as highly precise pseudo-range data. This technique allows the positional difference of the secondary GNSS antenna relative to the primary one to be determined with an accuracy of 2-10 millimeters, depending on environmental conditions. The accuracy of the heading angle estimation can be calculated using Equation 1 [11]:

$$\sigma_{\psi} = \sqrt{\frac{(\cos\psi)^2\,\sigma_e^2 + (\sin\psi)^2\,\sigma_n^2}{L^2(cos\theta)^2}}$$

Equation 1

σ_e and σ_n represent the accuracy of the relative displacement in the east and north directions between the two GNSS antennas, as determined by carrier phase differential positioning, while L is the distance between the two antennas. ψ is the GNSS compass heading and θ is the tilt angle.

Assuming σ_e , σ_n , and the GNSS system are operating under normal conditions, Equation 1 can be simplified, as shown in Equation 2 [11]:

$$\sigma_{\psi} = \frac{\sigma_h}{L}$$

Equation 2

σ_h is the accuracy of the relative displacement between the two antennas in the horizontal plane.

3. Data processing

The processing of the vehicle's trajectory data was performed using Qinertia post-processing software. This software integrates data from the MMS's positioning-related sensors including INS, GNSS, and Odometer (DMI) with base station data (Figure 8). The base station's coordinates can be defined as needed; in this study, they were referenced to the Royal Thai Survey Department's (RTSD) GNSS CORS network, which is the main agency with CORS installation in Thailand [24]. The data for each test area was processed twice, with the only difference being the configuration setting: once for a single- antenna (without Dual GNSS-estimated heading data) and once for a dual-antenna (with Dual GNSS-estimated heading data) (Figure 9). The front antenna served as the primary receiver. Post-Processing Kinematic (PPK) was selected as the processing method, PPK IonoShield Mode was selected as Auto, specifically with a tightly-coupled integration and combines the benefits of forward and backward processing (merge), which ultimately provides the smoothest and most accurate navigation solution. This choice was based on prior research by [25] and [26], which highlighted that PPK processing significantly improves result accuracy, and by [27], who demonstrated that tightly-coupled integration yields better and more accurate results than loosely-coupled integration. Commercial software processes the sensor data according to criteria specified by the software's developer and then exports the vehicle's trajectory as an ASCII text file with a data frequency of 200 Hz. As an INS-centric fusion, the output rate is the same as the IMU sampling rate.

Following data processing, the resulting vehicle trajectory files were analyzed with two main objectives: to evaluate the difference in vehicle orientation (heading/yaw), primarily by examining the Yaw value which indicates the direction of movement, and to assess the differences in Universal Transverse Mercator (UTM) coordinates (Northing, Easting, and Ellipsoidal height) across each survey area.

The results of the post-processing solution are typically categorized by status. PPK Fixed refers to a state where the software has successfully and confidently resolved the Integer Ambiguity, resulting in the highest positioning accuracy, typically at the centimeter or sub-centimeter level. Conversely, PPK Float indicates a state where the software has not been able to precisely and reliably resolve the Integer Ambiguity, yielding a lower accuracy that generally ranges from decimeter to meter.

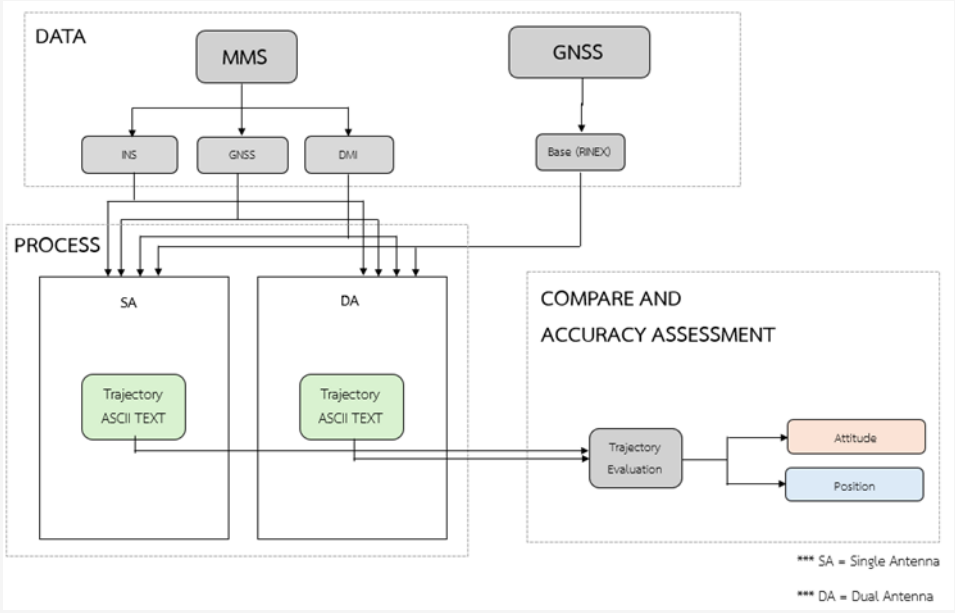

Figure 8: The block diagram of multi-sensor fusion systems in this study includes INS/GNSS (Single Antenna)/DMI and INS/GNSS (Dual Antenna)/DMI

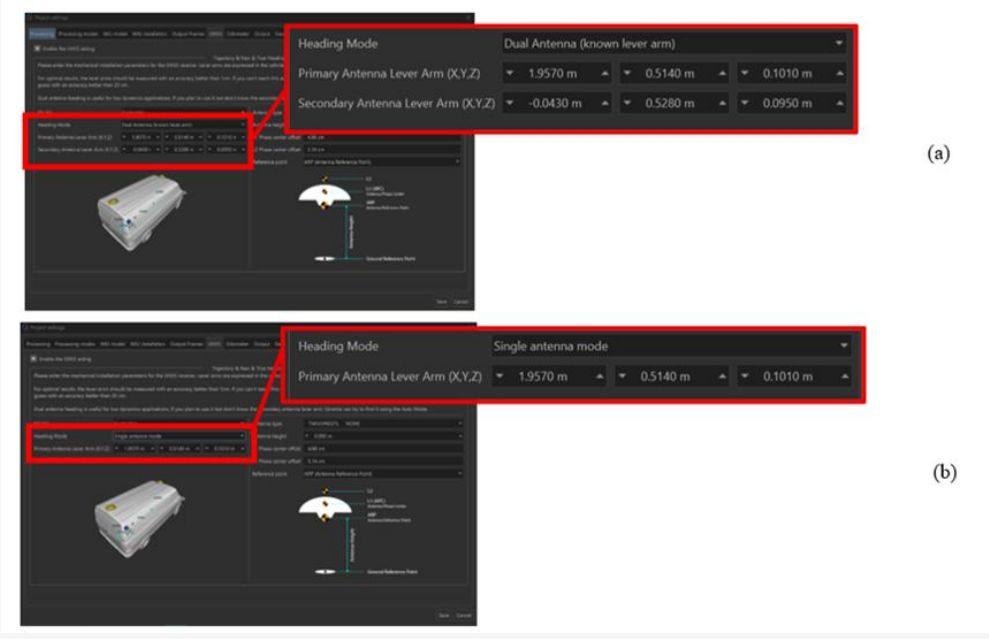

Figure 9: GNSS Antenna Mode Configuration in Qinertia software: (a) Dual-antenna and (b) Single-antenna

4. Results and Discussion

4.1 First Experiment: Urban Area

Following the data collection, a post-processing kinematic (PPK) analysis of the vehicle's trajectory was conducted, yielding distinct results based on the processing method. The solution type for urban areas is presented in Table 4. Because the GNSS data failed to satisfy the software's data selection criteria, which cannot be customized, other data was primarily utilized. The results indicate that there are periods where the solution relies primarily on data from auxiliary sensors rather than GNSS. This is because GNSS data does not meet the non-adjustable criteria of the processing software, requiring the reliance primarily on measurements from other integrated sensors, which is a limitation of the commercial software. The results indicate a minimal difference in overall solution type between the single-antenna and dual-antenna configurations. However, a noteworthy

observation is that the single-antenna configuration yielded a slightly higher percentage of Fixed solutions compared to the dual-antenna setup. This disparity may be attributable to the lower quality of GNSS data received by the auxiliary antenna, potentially due to signal obstructions encountered in the operational environment. Nevertheless, this marginal difference in solution type is insufficient to definitively conclude that the single-antenna system offers superior performance over the dual-antenna system.

Further analysis focused on the directional differences between the two processing methods. A plot was created to visualize the yaw difference between the single-antenna and dual-antenna results over the entire data collection period (Figure 10). The y-axis of this plot represented the difference in yaw values, while the x-axis indicated the time in seconds. The analysis of this data revealed minimal differences in yaw, with a maximum difference of 0.107°, a minimum difference of 0.000°, and a mean difference of 0.049°. Based on a paired t-test results, the calculated P-value ($p<0.001$) is substantially lower than the predetermined significance level ($\alpha = 0.05$). Consequently, we reject the null hypothesis (H_0). This result indicates that the observed difference between the Yaw values derived from the Single Antenna and Dual Antenna configurations is statistically significant and is not attributable to random chance.

Analysis using the commercial software identified two significant, consecutive periods of Dual GNSS-estimated heading data outage (Figure 11). The initial lapse, lasting six minutes (GPS time 120837 – 121207s), occurred when the Dilution of Precision (DOP) value began to exceed its average (Figure 3, Yellow highlight). The second, more extended period of 24 minutes (GPS time 123130 – 124592s) coincided with the peak DOP value in the area (Figure 3, Pink highlight). A comparative analysis with the yaw difference graph revealed a direct correlation: During the first outage (seconds 2360 – 2729), the yaw difference steadily increased while the Dual GNSS-estimated heading data was absent. Upon reacquisition, the yaw difference gradually converged (Figure 12). Conversely, during the second, more severe outage (seconds 4653 – 6115), the yaw difference exhibited significant volatility. Critically, after signal reacquisition, the Yaw divergence persisted for a duration before diminishing (Figure 13). This sustained divergence is attributed to the Extended Kalman filter (EKF)'s inherent mechanism within the Qinertia software [28], where the poor quality of the preceding data propagates estimation errors into subsequent epochs, causing a persistent but delayed convergence in the post-processed results. An analysis of Figure 13 shows a period from approximately 5350 to 5450 seconds (GPS time from 123827 to 123927 seconds) where the yaw difference decreases, indicating that the yaw values are becoming more similar. The processing results in the Qinertia software showed that, during this interval, the program relied mainly on odometer data (Figure 14(a)) to calculate the vehicle's trajectory for both single-antenna and dual-antenna processing. As noted earlier, the odometer contribution accounted for about 3.09%. This period also corresponds to when the vehicle was moving at a low speed or was stationary at times (Figure 14(b)).

Table 4: Solution type obtained by post-processing kinematic of urban are

Position (m.)	Dual-antenna (%)	Single-antenna (%)
PPK Fixed	73.6	74.96
PPK Float	20.99	19.64
Odometer	3.09	3.07
Zero Velocity Update (ZUPT)	2.31	2.32

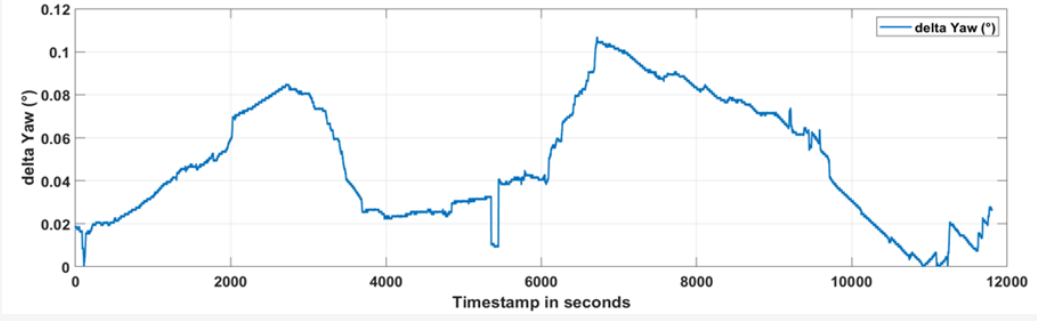

Figure 10: The Yaw difference between single antenna and dual antenna in urban area

Figure 11: The time interval of prolonged Dual GNSS-estimated heading data outage in urban area: (a) GPS time 120837 to 121207 seconds and (b) GPS time 123130 to 124592 seconds

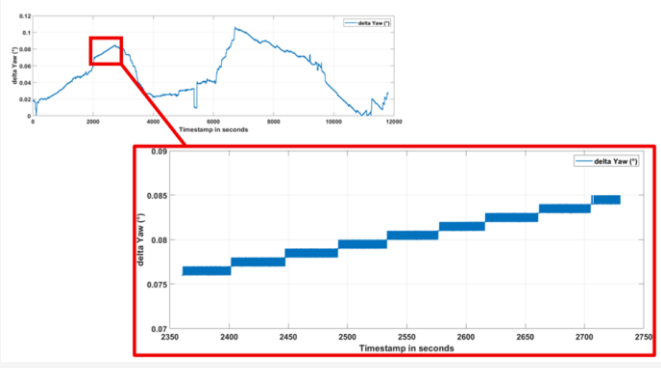

Figure 12: The Yaw difference between single antenna and dual antenna in urban area during the period GPS time 120837 to 121207 seconds

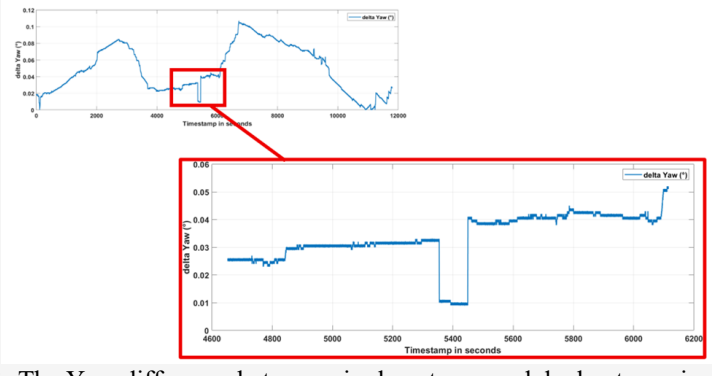

Figure 13: The Yaw difference between single antenna and dual antenna in urban area during the period GPS time 123130 to 124592 seconds

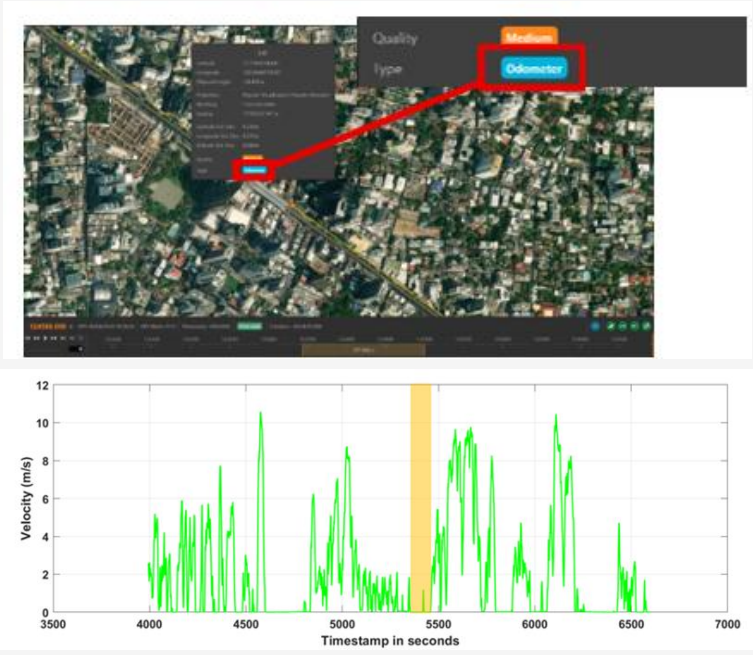

(a)

(b)

Figure 14: An investigation into the events occurring in the data during GPS time from 123827 to 123927 seconds: (a) Using data from the Odometer sensor (b) Vehicle velocity

Table 5: the difference in coordinate values in the UTM coordinate system of single antenna and dual antenna processing in the first experiment

Position (m.)	N	E	h	2D	3D
Min	0	0	0	0	0
Max	1.927	0.223	1.291	1.931	2.245
Mean	0.015	0.009	0.019	0.020	0.030
STD	0.082	0.025	0.076	0.085	0.113
RMSE	0.083	0.026	0.078	0.087	0.117

A comparison of the coordinates, specifically Northing, Easting, and Ellipsoidal height (Altitude), from the vehicle's trajectory file revealed notable differences. The mean Easting difference was 0.009 meters, with a maximum of 0.223 meters. In contrast, the maximum differences for Northing and Ellipsoidal height were 1.927 meters and 1.291 meters, respectively, as detailed in Table 5 It was observed that the areas with the largest height discrepancies primarily corresponded to a "float" solution type, where the GNSS data quality was classified as "Bad."

A graph in Figure 15 was plotted to visualize the differences in coordinate values over time. This allowed for a detailed examination of the discrepancies in each axis (Northing, Easting, and Altitude) throughout the data collection period. The analysis revealed two specific periods with high discrepancies in Northing, Easting, and ellipsoidal height. The first period was from 1658.52 to 1778.82 seconds (GPS time: 120135.52 – 120255.82 seconds). The second period was from 6047.01 to 6066.01 seconds (GPS time: 124524.01 – 124543.01 seconds). Both intervals coincided with a "Bad" GNSS status from the field data, and the vehicle's trajectory during these times was not a straight line, showing drift in coordinate values (Figure 16). Given that the vehicle's trajectory primarily follows an East-West orientation, the Northing component is critically sensitive to the accuracy of the Heading (Yaw) angle. Any uncorrected or persistent error in the estimated Yaw angle even a minor one is directly projected onto the North position. When GNSS data quality drops, the INS's drift in Yaw is less effectively constrained by the filter in the North direction, leading to a much faster and greater accumulation of position error in the Northing component.

When processing georeferenced point cloud data using trajectory files from both single-antenna and dual-antenna processing, the differences can be seen as shown in the Figure 17. The results of the georeferenced point cloud from the single-antenna configuration are more scattered and have more position errors than the results from the dual-antenna configuration, which is consistent with the results of [11].

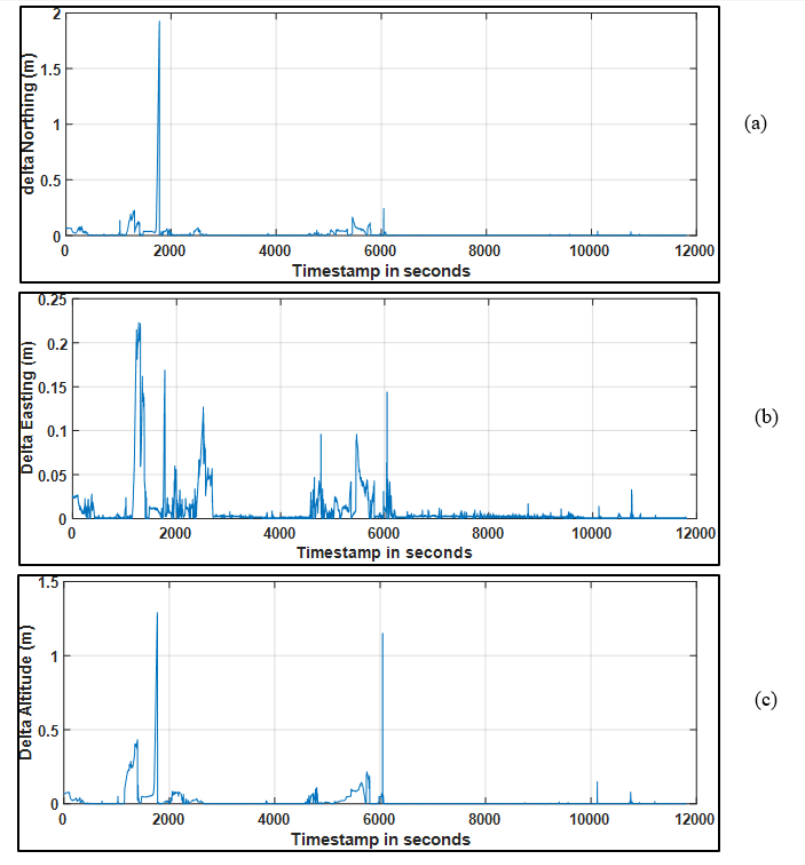

Figure 15: The difference in location coordinate between single antenna and dual antenna in urban area: (a) Delta Northing, (b) Delta Easting and (c) Delta Altitude

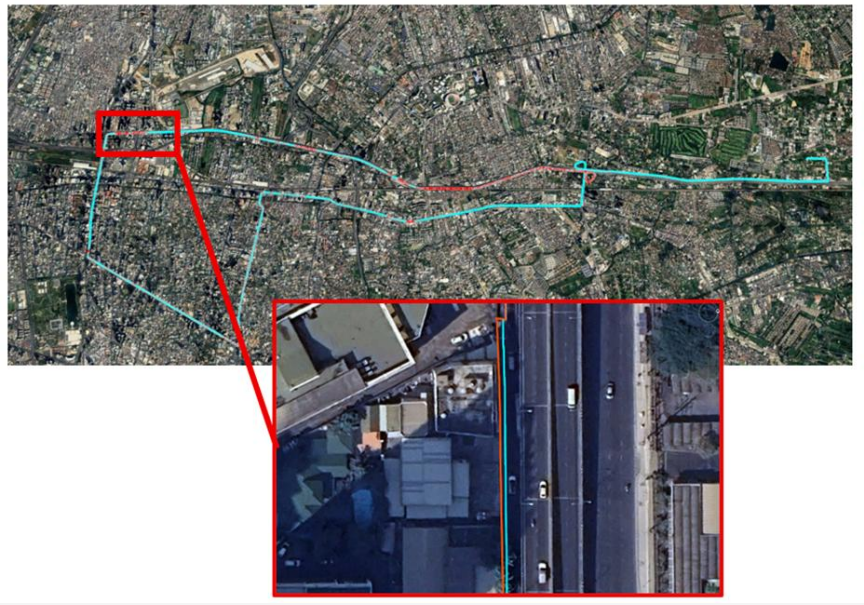

Figure 16: Trajectory result at urban area (red) Single-antenna trajectory, (blue) Dual-antenna trajectory

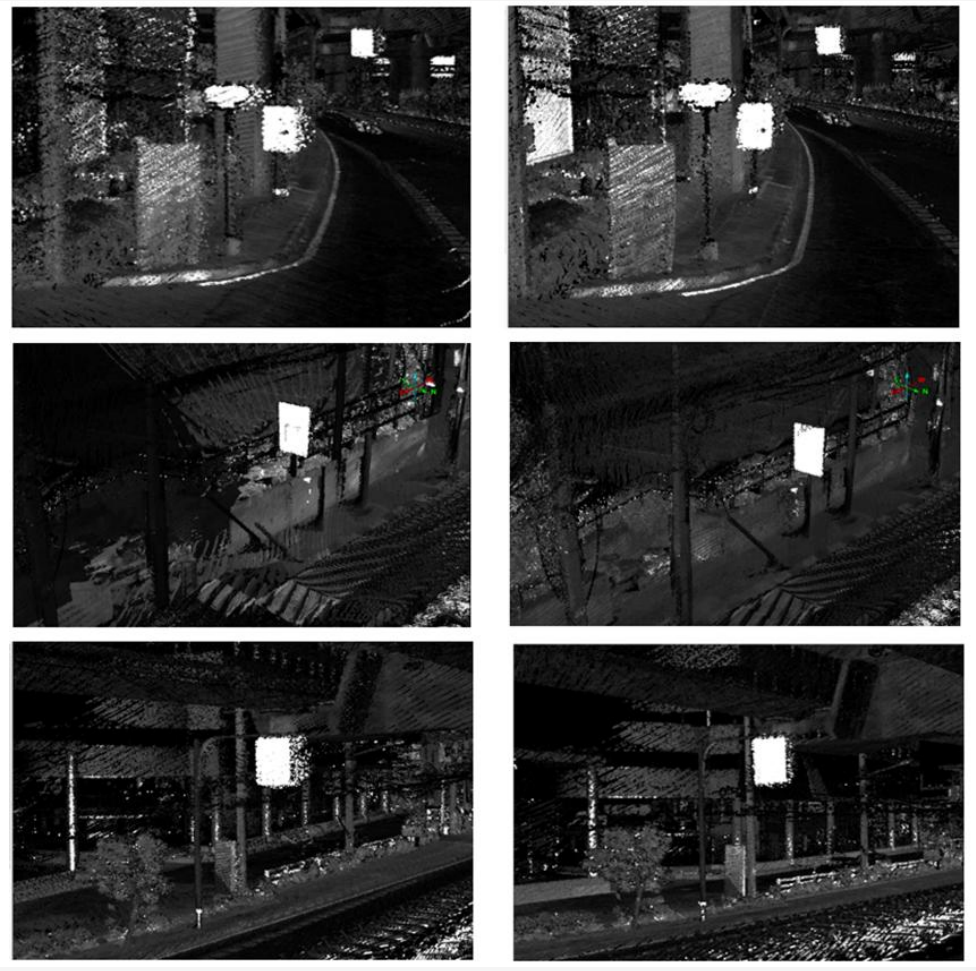

(a) (b)

Figure 17: Georeferenced point cloud of the experiment in urban area
(a) single antenna (b) dual antenna

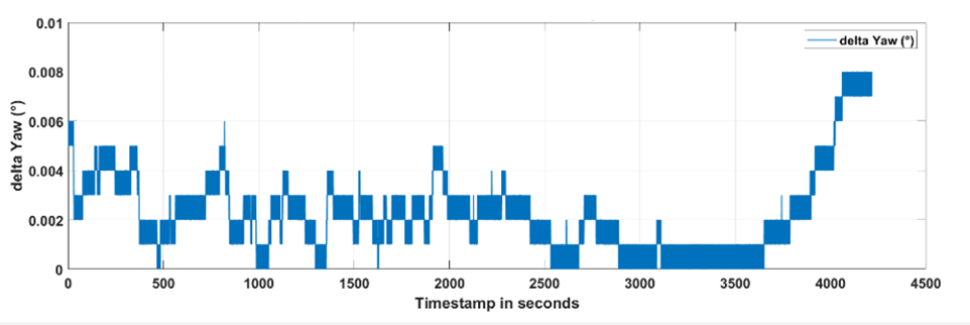

Figure 18: The Yaw difference between single antenna and dual antenna in open-sky area

4.2 Second Experiment: Open-sky Area

Post-processing kinematic (PPK) results for both single-antenna and dual-antenna configurations yielded a high-quality status, with PPK Fixed at 99.61% and PPK Float at 0.40%. An analysis of the directional differences was performed by plotting the yaw differences between the single-antenna and dual-antenna processing results (Figure 18) over the entire data collection period in the second experiment. The analysis showed a high level of consistency, with a maximum difference of 0.008°, a minimum difference of 0.000°, and a mean difference of 0.002°. Based on the paired t-test results, the calculated P-value ($p = 0.00136$) is substantially lower than the predetermined significance level ($\alpha = 0.05$), leading to the rejection of the null hypothesis (H_0). This

indicates that the observed difference is statistically robust and confirms that the two compared outputs are genuinely distinct. However, when considering the high volume of data used in the analysis, the magnitude of this statistically significant difference is practically very small.

A comparison of the coordinate positions revealed very minimal differences (Figure 19), measuring in the sub-millimeter range, as detailed in Table 6. The graphs in Figure 20 were plotted to visualize the coordinate differences within the UTM coordinate system, which revealed the discrepancies in each axis over time. It can be seen that the difference across all three axes (Northing, Easting and Altitude) is within a maximum of 1 mm. This difference in value is sufficiently small to be considered practically insignificant. When processing georeferenced point cloud data using trajectory files from both single-antenna and dual-antenna processing, the differences can be seen as shown in the Figure 21. There is no visible difference between the two overall georeferenced point cloud.

Figure 19: Trajectory result at open-sky area (red) Single-antenna trajectory (blue) Dual-antenna trajectory

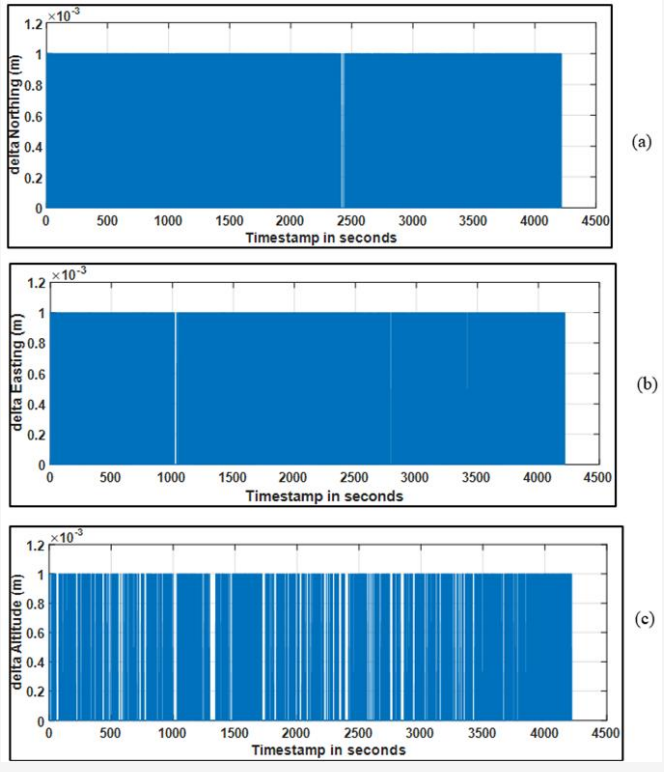

Figure 20: The difference in location coordinate between single antenna and dual antenna in open-sky area: (a) Delta Northing (b) Delta Easting (c) Delta Altitude

Table 6: the difference in coordinate values in the UTM coordinate system of single antenna and dual antenna processing in open-sky area

Position (m.)	N	E	h	2D	3D
Min	0	0	0	0	0
Max	0.001	0.001	0.001	0.001	0.002
Mean	5.1823×10^{-5}	4.9081×10^{-5}	2.7188×10^{-6}	9.9246×10^{-5}	1.0178×10^{-4}
STD	2.2167×10^{-4}	2.1604×10^{-4}	5.2071×10^{-5}	3.0175×10^{-4}	3.0539×10^{-4}
RMSE	2.2765×10^{-4}	2.2154×10^{-4}	5.2142×10^{-5}	3.1765×10^{-4}	3.2190×10^{-4}

(a) (b)

Figure 21: Georeferenced point cloud of the experiment in open-sky condition using different antenna configurations (a) single antenna (b) dual antenna

5. Conclusion

This study rigorously evaluated the performance differences between single-antenna and dual-antenna Tight coupling Post-Processing Kinematics (PPK) configurations. Although overall trajectory differences were invisible to the naked eye, detailed analysis revealed measurable variations in both yaw and position accuracy, particularly when operating in complex urban environments. These findings highlight the sensitivity of attitude estimation to GNSS signal stability and the chosen processing strategy. The findings also emphasize that the reliability of dual-GNSS orientation estimation depends not only on signal availability but also on the system's ability to efficiently recover from data loss via an Extended Kalman Filter (EKF). This has practical implications for mobile mapping and navigation applications where intermittent GNSS reception is unavoidable. Therefore, it is recommended that adequate data collection planning be undertaken prior to field data collection to minimize orientation errors and improve the quality of acquired destination information, such as point cloud accuracy. Furthermore, the resulting point cloud quality showed that using the dual-antenna configuration in urban areas can yield better results than using the single-antenna configuration. Overall, this study demonstrates that environmental context and GNSS signal stability are key factors that determine vehicle orientation and position accuracy. While dual-antenna systems can improve stability, their benefits are diminished under conditions of

severe noise. Limitations of this research include the lack of defined absolute accuracy for each processing method. And by focusing only on PPK with tight coupling without evaluating alternative processing strategies such as PPP or loose coupling, future research should extend this comparative analysis to include these methods to develop a more comprehensive understanding of multi-antenna performance under various GNSS conditions.

Acknowledgements
The author would like to express sincere gratitude to **VSK Global Co., Ltd.** for their invaluable support in providing the data and processing software used in this research. Their contribution was crucial to the completion of this study and is highly appreciated.

References

[1] Elhashash, M., Albanwan, H. and Qin, R., (2022). A Review of Mobile Mapping Systems: From Sensors to Applications. *Sensors*, Vol. 22(11). https://doi.org/10.3390/s22114262.

[2] Noureldin, A., Karamat, T. B. and Georgy, J., (2012). *Fundamentals of Inertial Navigation, Satellite-based Positioning and their Integration*. Springer Berlin Heidelberg. https://doi.org/10.1007/978-3-642-30466-8.

[3] Srinara, S., Chiu, Y. T., Tsai, M. L. and Chiang, K. W., (2022). High-definition Point Cloud Map-based 3D LiDAR-IMU Calibration for Self-driving Applications. *The International Archives of the Photogrammetry, Remote Sensing and Spatial Information Sciences*, Vol. 43; 271-277. https://doi.org/10.5194/isprs-archives-XLIII-B1-2022-271-2022.

[4] Angelats, E. and Colomina, I., (2014). One Step Mobile Mapping Laser and Camera Data Orientation and Calibration. *The International Archives of the Photogrammetry. Remote Sensing and Spatial Information Sciences*, Vol. 40,15-20. https://doi.org/10.5194/isprsarchives-XL-3-W1-15-2014.

[5] Fukano, K. and Masuda, H., (2015). Detection and Classification of Pole-like Objects from Mobile Mapping Data. ISPRS Annals of the Photogrammetry. *Remote Sensing and Spatial Information Sciences*, Vol. 2, 57-64. https://doi.org/10.5194/isprsannals-II-3-W5-57-2015.

[6] Gorte, B., Oude Elberink, S., Sirmacek, B. and Wang, J., (2015). IQPC 2015 Track: Tree Separation and Classification in Mobile Mapping Lidar Data. *The International Archives of the Photogrammetry, Remote Sensing and Spatial Information Sciences*, Vol. 40, 607-612. https://doi.org/10.5194/isprsarchives-XL-3-W3-607-2015.

[7] Choi, I. H. and Kim, E. M., (2022). Automatic Construction of Road Lane Markings Using Mobile Mapping System Data. *Sensors & Materials*, Vol. 34, 1-11, https://sensors.myu-group.co.jp/sm_pdf/SS3872.pdf.

[8] Sairam, N., Nagarajan, S. and Ornitz, S., (2016). Development of Mobile Mapping System for 3D Road Asset Inventory. *Sensors*, Vol. 16(3). https://doi.org/10.3390/s16030367.

[9] Sa-ngiam, N., (2020). The Development of Calibration Systems and Techniques to Create High-accuracy 3D Maps for the Hydro and Agro Informatics Institute (Public Organization). *The 25th National Convention on Civil Engineering*, Vol. 25, SGI15–SGI15.

[10] Zhu, F., Hu, Z., Liu, W. and Zhang, X., (2019). Dual-antenna GNSS Integrated with MEMS for Reliable and Continuous Attitude Determination in Challenged Environments. *IEEE Sensors Journal*, Vol. 19(9), 3449-3461. https://doi.org/10.1109/JSEN.2019.2891783.

[11] Brazeal, R. G., Wilkinson, B. E. and Benjamin, A. R., (2021). Investigating Practical Impacts of Using Single-antenna and Dual-antenna GNSS/INS Sensors in UAS-Lidar Applications. *Sensors*, Vol. 21(16). https://doi.org/10.3390/s21165382.

[12] Cui, B., Zhang, J., Wei, X., Cui, X., Sun, Z., Zhao, Y. and Liu, Y., (2024). Improved Information Fusion for Agricultural Machinery Navigation Based on Context-Constrained Kalman Filter and Dual-Antenna RTK. *Actuators*, Vol. 13(5). https://doi.org/10.3390/act13050160.

[13] Jin, W., Gong, W., Hou, T., Sun, X. and Ma, H., (2023). A Dual-antenna Heading Determination Method for Single-frequency GNSS Antennas with Large Phase Pattern Variations. *GPS Solutions*, Vol. 27(2). https://doi.org/10.1007/s10291-023-01429-1.

[14] Liu, Z. and Pan, W., (2025). Enhancing Navigation Control Accuracy of Guidance Line Drawing Robot by Dual Antenna GNSS and MEMS IMU. *Scientific Reports*, Vol. 15(1). https://doi.org/10.1038/s41598-025-11207-3.

[15] Deppe, O., Dorner, G., König, S., Martin, T., Voigt, S. and Zimmermann, S., (2017). MEMS and FOG Technologies for Tactical and Navigation Grade Inertial Sensors Recent Improvements and Comparison. *Sensors*, Vol. 17(3). https://doi.org/10.3390/s17030567.

[16] Al Bitar, N. and Gavrilov, A., (2021). A New Method for Compensating the Errors of Integrated Navigation Systems Using Artificial Neural Networks. *Measurement*, Vol. 168. https://doi.org/10.1016/j.measurement.2020.108391.

[17] Jouybari, A., Bagherbandi, M. and Nilfouroushan, F., (2023). Numerical Analysis of GNSS Signal Outage Effect on EOPs Solutions Using Tightly Coupled GNSS/IMU Integration: A Simulated Case Study in Sweden. *Sensors*, Vol. 23(14). https://doi.org/10.3390/s23146361.

[18] Paijitprapaporn, C., Thongtan, T. and Satirapod, C., (2021). Accuracy Assessment of Integrated GNSS Measurements with LIDAR Mobile Mapping Data in Urban Environments. *Measurement: Sensors*, Vol. 18. https://doi.org/10.1016/j.measen.2021.100078.

[19] Wu, J., Jiang, J., Zhang, C., Li, Y., Yan, P. and Meng, X., (2023). A Novel Optimal Robust Adaptive Scheme for Accurate GNSS RTK/INS Tightly Coupled Integration in Urban Environments. *Remote Sensing*, Vol. 15(15). https://doi.org/10.3390/rs15153725.

[20] He, Y., Li, J. and Liu, J., (2023). Research on GNSS INS & GNSS/INS Integrated Navigation Method for Autonomous Vehicles: A Survey. *IEEE Access*, Vol. 11, 79033-79055.

[21] Ye, H., Chen, Y. and Liu, M., (2019). Tightly Coupled 3d Lidar Inertial Odometry and Mapping. *International Conference on Robotics and Automation (ICRA)*. 3144-3150, https://doi.org/10.1109/ICRA.2019.8793511.

[22] Hoang, M. L. and Pietrosanto, A., (2021). Yaw/Heading Optimization by Drift Elimination on MEMS Gyroscope. *Sensors and Actuators A: Physical*, Vol. 325. https://doi.org/10.1016/j.sna.2021.112691.

[23] Glabe, J., (2021). *Euler Angles and Roll Pitch Yaw Representation, Encyclopedia of Robotics*, Springer.

[24] Rizos, C. and Satirapod, C., (2011). Contribution of GNSS CORS Infrastructure to the Mission of Modern Geodesy and Status of GNSS CORS in Thailand. *Engineering Journal*, Vol. 15(1), 25-42. https://doi.org/10.4186/ej.2011.15.1.25.

[25] Iizuka, K., Ogura, T., Akiyama, Y., Yamauchi, H., Hashimoto, T. and Yamada, Y., (2022). Improving the 3D Model Accuracy with a Post-processing Kinematic (PPK) Method for UAS Surveys. *Geocarto International*, Vol. 37(14), 4234-4254. https://doi.org/10.1080/10106049.2021.1882004.

[26] Bannakulpipat, T., (2023). Improvement of Positional Accuracy of Unmanned Aerial Vehicle-based Satellite Navigation Data for Mapping Applications. *Engineering Journal of Research and Development*, Vol. 34(3), 23-37.

[27] Cioffi, G. and Scaramuzza, D., (2020). Tightly-coupled Fusion of Global Positional Measurements in Optimization-based Visual-inertial Odometry. *2020 IEEE/RSJ International Conference on Intelligent Robots and Systems (IROS)*. 5089-5095. https://doi.org/10.1109/IROS45743.2020.9341697.

[28] Lever Arm Estimation. *SBG Support Center*. [Online]. Available: https://support.sbg-systems.com/sc/qd/latest/reference-manual/lever-arm-estimation. [Accessed Oct. 15, 2025].